Thermal runaway propagation behavior within 18,650 lithium-ion battery packs: A modeling study

Yikai Jia[a,b], Mesbah Uddin[a], Yangxing Li[a,*], Jun Xu[a,b,*]

[a] Department of Mechanical Engineering and Engineering Science, The University of North Carolina at Charlotte, Charlotte, NC 28223, USA
[b] Vehicle Energy & Safety Laboratory (VESL), North Carolina Motorsports and Automotive Research Center, The University of North Carolina at Charlotte, Charlotte, NC 28223, USA

ARTICLE INFO

ABSTRACT

Thermal runaway and subsequent propagation are the main factors to cause catastrophic consequences in lithium-ion battery packs. Exploring the thermal runaway propagation is thus of great fundamental and practical interest in understanding the mechanism of battery safety. A thermal runaway propagation mathematical model is established by combining the 0 D thermal runaway, and electrical and thermal conduction models that are verified by a series of experiments where thermal runways are triggered by mechanical abusive loading. Two thermal runaway propagation modes are observed and it is found that overheating of the local area or high overall temperature determines the propagation mode. The governing factors of thermal runaway propagation speed, including ambient temperature, packing spacing, and stacking form, are further analyzed. Our analysis reveals a complete link between engineering design variables and the thermal runaway behaviors of a specific battery pack. Our study paves a novel avenue to design the safer and higher energy density lithium-ion battery pack and elevates the limits of battery pack energy density without sacrificing safety risks.

Nomenclature

Parameter	Description	Value	Unit	Source
A_a	Frequency factor for anode decomposition	$2.5 \cdot 10^{13}$	s^{-1}	Ref [1].
A_c	Frequency factor for cathode decomposition	$6.67 \cdot 10^{11}$	s^{-1}	Ref [1].
A_{ec}	Frequency factor for electrochemical reactions	$3.37 \cdot 10^{12}$	s^{-1}	Ref [2].
A_s	Frequency factor for SEI decomposition	$1.67 \cdot 10^{15}$	s^{-1}	Ref [1].
A_e	Frequency factor for electrolyte decomposition	$5.14 \cdot 10^{25}$	s^{-1}	Ref [3].
C	Capacity of battery	3.35	Ah	Meas.
V	Nominal voltage of cell	4.2	V	Meas.
E_a	Activation energy for anode decomposition	$2.24 \cdot 10^{-19}$	J	Ref [1].
E_c	Activation energy for cathode decomposition	$2.03 \cdot 10^{-19}$	J	Ref [1].
E_{ec}	Activation energy for short circuit	$1.58 \cdot 10^{-19}$	J	Ref [2].
E_s	Activation energy for SEI decomposition	$2.24 \cdot 10^{-19}$	J	Ref [1].
E_e	Activation energy for electrolyte decomposition	$4.55 \cdot 10^{-19}$	J	Ref [3].
h_a	Enthalpy of anode decomposition reaction	1714	Jg^{-1}	Ref [1].
h_c	Enthalpy of cathode decomposition reaction	314	Jg^{-1}	Ref [1].
h_{ec}	Heat released by short-circuit	10.17	kJ	Calc.
h_s	Enthalpy of SEI decomposition reaction	257	Jg^{-1}	Ref [1].
h_e	Enthalpy of electrolyte decomposition reaction	155	Jg^{-1}	Ref [3].
m_a	Mass of anode	$8.1 \cdot 10^{-3}$	kg	Ref [4].
m_c	Mass of cathode	$18.3 \cdot 10^{-3}$	kg	Ref [4].
x_a	Fraction of Li in anode	$x_{a0} = 0.75$	–	Ref [1].
x_s	Fraction of Li in SEI	$x_{s0} = 0.15$	–	Ref [1].
α_c	Initial degree of conversion of cathode	$\alpha_{c0} = 0.04$	–	Ref [1].
z	Dimensionless measure of SEI thickness	$z_0 = 0.033$	–	Ref [1].
c_e	Dimensionless concentration of electrolyte	$c_{e0} = 0.033$	–	Ref [3].
η	Efficiency factor	0.45	–	Fit.
ρ_{jr}	Density of jellyroll	2580	kgm^{-3}	Ref [1].
ρ_{shell}	Density of shell	7800	kgm^{-3}	Approx.
$c_{p,jr}$	Specific heat capacity of jellyroll	2580	kgm^{-3}	Ref [1].
$c_{p,shell}$	Specific heat capacity of shell	7800	kgm^{-3}	Approx.
V_{cell}	Volume of cell	$1.663 \cdot 10^{-5}$	m^3	Calc.
R_r	Internal resistance of battery	40	$m\Omega$	Meas.

* Corresponding author.
E-mail addresses: yli117@uncc.edu (Y. Li), jun.xu@uncc.edu (J. Xu).

R_{isc}	Equivalent resistance of short-circuit	90	mΩ	Fit.
R_{inner}	Inner radius of jellyroll	1.125	mm	Meas.
R_{outer}	Outer radius of jellyroll	9	mm	Meas.
h	Thickness of battery shell	0.11	mm	Meas.
L	Length of battery	65	mm	Approx.
θ_c	Equivalent thermal resistance between two batteries	$f(d)$	K/W	Approx.
θ_p	Equivalent thermal resistance between battery shell and jellyroll	0.0363	K/W	Approx.
h_{conv}	Convection heat dissipation coefficient	10	W/(K·m^2)	Approx.

1. Introduction

Lithium-ion batteries (LIBs) have now been used increasingly predominant in vehicle markets. Large packs of batteries in electric vehicles experience harsh environments, e.g., mechanical [5-11] thermal [2, 12] and electrical [13, 14] abusive loading, which can lead to short circuits and thus causes deteriorated performance, fire, and explosion [5, 15-19]. Thermal runaway (TR) is one of the most severe consequences that could cause fatality incidents. To manage and predict this dangerous process, an efficient model is desired to be established. Recently, the mechanisms of thermal reactions are continually studied and gradually unraveled. Based on the theories of thermal reactions, many TR models have been established based on theoretical equations and finite element (FE) computational techniques. Hatchard et al. [1] proposed a TR model of 18,650 LCO LIB based on Arrhenius formulations and provided related activation energies and the enthalpies of various decomposition reactions for the compounds. Moreover, several decomposition reactions were further considered in this model, whereas high-dimension models were built [3]. Based on the TR models and theories, Coman et al. [2] provided a brief computational framework for predicting the TR behavior of 18,650 LIBs.

When the TR of the first battery of a battery pack is triggered, the neighboring batteries will be heated and probably triggered to yield runaway reactions in some specific scenarios [20, 21]. This phenomenon, called TR propagation, can lead to catastrophic hazards within battery packs [22, 23]. To determine the behavior and mechanisms underlying this phenomenon, several theoretical and numerical were experiments conducted. Numerous experiments show that thermal conduction, thermal radiation, and thermal accumulation during fire heating are three important factors for TR propagation, no matter for cylindrical cells [24], prismatic cells [25, 26] or pouch cells [27]. Among these factors, thermal contact [28], interspacing and appropriate fire retardant materials between the cells are required to hinder fire propagation [21, 29]. Based on the experimental results of an ISO 9705 Full-Scale Room Fire test, Huang et al. [12] gave a theoretical analysis of the TR propagation of a 2-cylindrical-cell system and came up with the self-accelerating decomposition temperature. Similarly, Feng et al. [30, 31] established a 3D finite element model (FEM) of a large-scale format battery pack based on the experiment for safe battery pack design.

Nevertheless, several intrinsic shortages are observed in the currently available discussions and established models. First of all, the fundamental TR propagation modes are still unraveled, hindering the accurate prediction of runaway propagation within one battery pack and thus leaving an unsolved headache for thermal spread prevention design. Secondly, using finite element analysis with the TR model takes extremely high computational resources (six battery cells with more than 37,000 tetrahedral elements, in the FE model and 670,000 degrees of freedom, in the model [30]).In the real-world, the battery pack for a Tesla car consists of more than 7000 cylindrical cells; and different formats of batteries, i.e., cylindrical [12], prismatic and pouch cell [29] may use different modeling strategy to enabling an excellent computational convergence.

To bridge this gap, in this study, an efficient yet accurate

computational framework is constructed based on theoretical analysis. The established mathematical model was validated by a series of mechanically triggering runaway propagation tests; two major thermal spread modes were consequently discovered; governing factors were discussed; and therefore, the TR propagation mechanism was fully revealed to some extend.

2. Methods

2.1. Experimental battery samples

The battery used in this study is a widely commercialized NCA 18,650 lithium-ion battery, namely, the Panasonic NCR 18,650–B, which possesses NCA/graphite as electrodes. The nominal capacity of this battery is 3350 mAh, and its charge/discharge cutoff voltages are 4.2 and 2.5 V, respectively. The cell mainly consists of a jellyroll, an inside winding nail, and a steel shell. The jellyroll consists of anode and cathode materials, separators, current collectors, and electrolytes. In general, the electrolyte is dissolved LiPF$_6$ salt in carbonate solvents [32]. All brand-new batteries are charged to full SOC by a BK6808AR rechargeable battery performance tester.

2.2. Thermal runaway propagation experiment design

TR propagation tests were performed in an explosion-proof fume hood fixed in a universal material test machine, namely, the SANS UTM5000 (Fig. 1). The plastic outer skin of each battery was peeled away. Specific numbers of single batteries were tied by some slender copper wires and then painted by black high-temperature paint to form the battery pack used in this study. In some cases, the batteries of each pack were connected by nickel sheets in parallel. During the tests, one of the batteries in each pack was penetrated by a 2 mm diameter needle with a 6 mm/min loading rate. Simultaneously, a camera was used to record the experimental phenomena. An infrared thermal imager was used to measure the surface temperature distribution through an infrared transparent sapphire window on the explosion-proof fume hood. A multimeter Agilent 34970A was applied to collect the voltage data of the battery pack. K-type thermocouples were placed at the axial midpoints on the surface of batteries. The temperature contribution of each battery is assumed that satisfies the lumped model [12]. Therefore, the measured temperatures were the average temperatures of the batteries. The batteries were tied with copper wire with some pre-pressure. The battery numbers are defined as Fig. 1. In order to facilitate the establishment of the model, the battery pack in this paper is a kind of idealized battery pack, related fixed structures and other parts in battery modules are ignored. The contact relationship among batteries will be abstracted into several equivalent thermal resistances.

2.3. Establishment of the thermal runaway propagation model

A multi-node numerical model and the balance of energy are adopted to calculate the average temperature of each battery. This approximation for small batteries like 18,650 has been verified that it is reasonable [33, 34]. To take the thermal contact among the battery into account, the cell jellyroll is considered as a node while the battery shell was divided into several nodes according to the pack form. (Fig. 2a–b). Each node is connected to other nodes through the equivalent thermal resistance.

For each jellyroll node, the heat produced during the ISC and TR processes (consisting of the Joule heat and the exothermic reaction heater source) is set as its heat sources. The exothermic reaction heater source is calculated by an electrochemical model of a single cell jellyroll domain that is established using Arrhenius equations [2, 35].
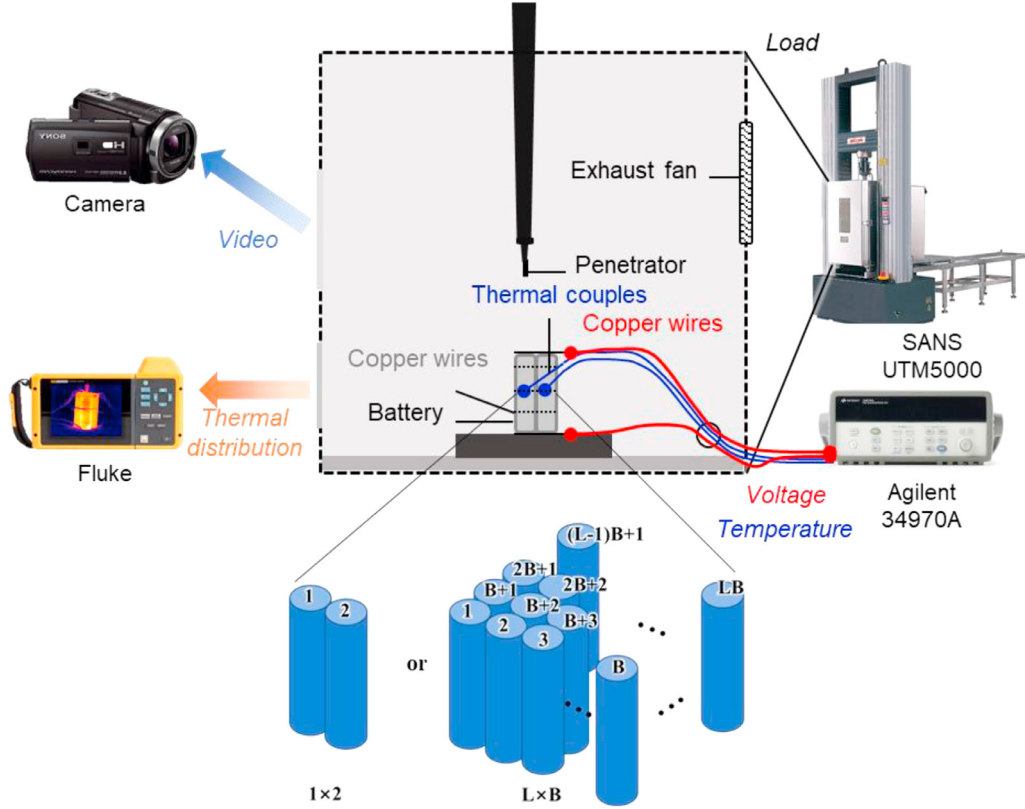
The equation of energy balance can be written as follows:

Fig. 1. Schematic illustration of the penetration test's experimental method. Experimental equipment, design and the definition of battery numbers in this paper.

$$\rho C_{p,jr} \, dT_i/dt = \dot{Q}_{exo,i} + \sum_k \dot{Q}_{con\_inner,i,k} + \dot{Q}_{joule,i},$$

(1)

where the terms ρjr (kg/mm²), $C_{p,\,jr}$(J/K), T (K) are the average density,

the total heat capacity and the average temperature of jellyroll, respectively.

The chemical reaction rates $\dot{Q}_{exo,i}$ of a single cell jellyroll domain are calculated by using Arrhenius equations as follows [2, 35]:
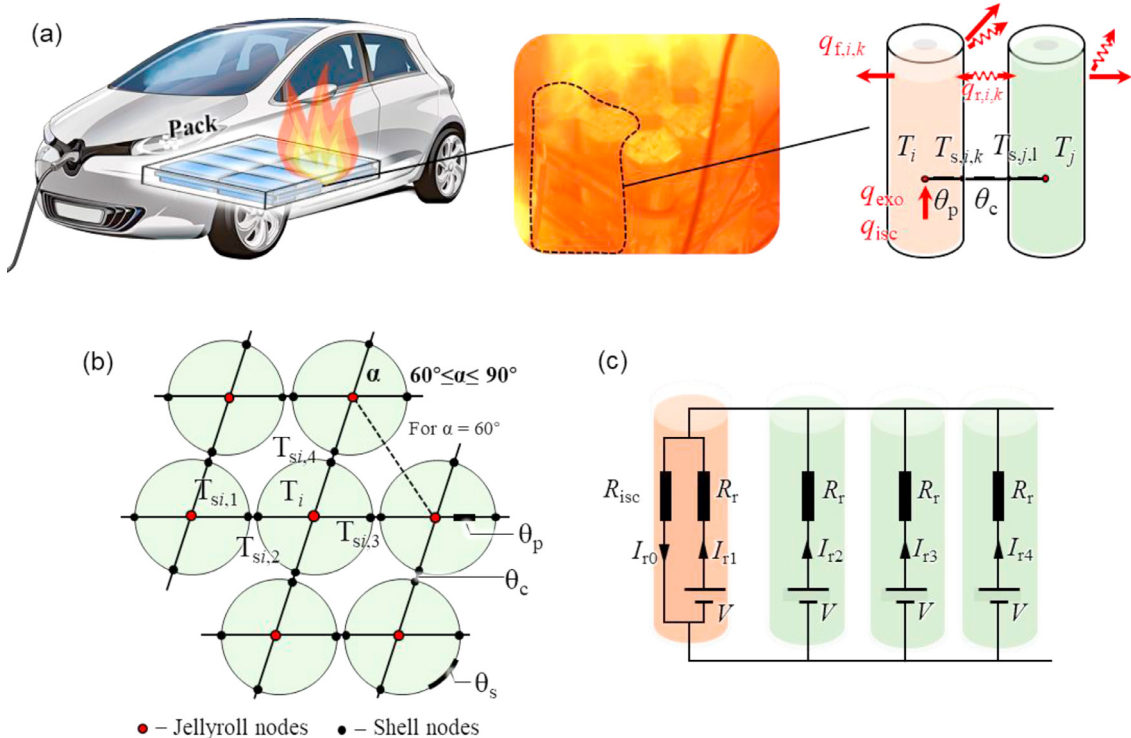

Fig. 2. Schematic of the TR propagation model. (a) The thermal equivalent method of a single battery and links among cells; (b) Node division method; (c) Schematic of the electric connections.

$$dx_a/dt = -x_a \cdot A_a \cdot \exp(-E_a/k_b T) \cdot \exp(-z/z_0), \tag{2}$$

$$dz/dt = x_a \cdot A_a \cdot \exp(-E_a/k_b T) \cdot \exp(-z/z_0), \tag{3}$$

$$dx_s/dt = -x_s \cdot A_s \cdot \exp(-E_s/k_b T), \tag{4}$$

$$d\alpha/dt = \alpha \cdot (1 - \alpha) \cdot A_c \cdot \exp(-E_c/k_b T), \tag{5}$$

$$dc_e/dt = -A_e \cdot \exp(-E_e/k_b T), \tag{6}$$

$$dSoC/dt = -ISC_{cond} \cdot SoC \cdot A_{ec} \cdot \exp(-E_{ec}/k_b T). \tag{7}$$

Eqns. (2)–6 describe the decomposition reaction. T is the average temperature of the cell. x_a and x_s represent the fractions of Li-ion present in the anode and solid electrolyte interphase (SEI), respectively. α is the degree of conversion of the cathode. z is the SEI thickness according to the tunneling effect [36, 37]. c_e is the dimensionless concentration of the electrolyte. Eq. (7) estimates the SOC [38]. The term ISC_{cond} is used to control the triggering of the battery ISC. The ISC triggering condition is set as when the temperature of the jellyroll node reaches the separator melting point [39, 40] (165 °C for the chosen battery). The ISC of the first battery was triggered manually in the model ($ISC_{cond}=1$ for the first battery).

The exothermic reaction heater source $\dot{Q}_{exo,i}$ is defined as follows [2]:

$$\dot{Q}_{exo,i} = \dot{Q}_a + \dot{Q}_c + \dot{Q}_s + \dot{Q}_e + \dot{Q}_{ec}, \tag{8}$$

$$\dot{Q}_a = -m_a h_a dx_a/dt, \tag{9}$$

$$\dot{Q}_c = m_c h_c d\alpha/dt, \tag{10}$$

$$\dot{Q}_s = -m_s h_s dx_s/dt, \tag{11}$$

$$\dot{Q}_e = -m_e h_e dc_e/dt, \tag{12}$$

$$\dot{Q}_{ec} = -h_{ec} dSoC/dt. \tag{13}$$

Eqns. (9)–12 describe the heat release rate of decomposition reactions. Eq. (13) illustrates the heat release rate of electrical–thermal conversion during discharging. The enthalpies in Eqns. (9)–12 have been given by references, as shown in the nomenclature. The enthalpy in Eq. (13) is given as follows [2]:

$$h_{ec}=3600VC\eta, \tag{14}$$

where V is the nominal discharge voltage, and C is the nominal battery capacity. η is the efficiency factor that represents how much electrical energy is converted to thermal energy. In this model, $\eta= 0.47$ was obtained by matching the peak temperature of the experiment. Thus, the exothermic reaction power is determined by the instantaneous SOC and Temperature.

The term $\dot{Q}_{joule,i}$ represents the joule heat during the discharge produced by the ISC or ISC-triggered batteries in the same parallel connection module. The Joule heat can be calculation by Joule's law and Ohm's law [41]. For a parallel-connected battery system with several batteries (Fig. 2c). If the battery number is N, the short-circuit current can be written as follows:

$$I_{r0} = \sum_{i-1}^{n} I_{ri}, \tag{15}$$

$$I_{ri} = V/(N \cdot R_{isc} + R_r). \tag{16}$$

Furthermore, joule heats are calculated as follows:

$$\dot{Q}_{joule,1} = (V/(N \cdot R_{isc} + R_r))^2 \cdot (N^2 R_{isc} + R_r) \cdot (1 - ISC_{cond}), \tag{17}$$

$$\dot{Q}_{joule,i} = (V/(N \cdot R_{isc} + R_r))^2 \cdot R_r \cdot (1 - ISC_{cond}), \ i = 2, 3. ..N, \tag{18}$$

where the term 1-ISC_{cond} means that if TR occurs and the separator starts melting, this mechanical ISC discharging would be terminated. Note that the additional thermal resistance brought by the wires is ignored.

For other nonparallel connected situations, the ISC-triggered battery

has no electrical connection with surrounding batteries. Thus, the joule heat can be calculated by Eq. (28) in N = 1. For the first battery, when $SoC=0$, the ISC heater $\dot{Q}_{joule,1}$ will be set as 0.

$\dot{Q}_{conv\_inner,i,k}$ is the heat transfer between the jellyroll node i and the shell node k of battery i. Thermal resistance θ_p is set among the jellyroll and shell nodes. $\dot{Q}_{conv\_inner,i,k}$ can be written as follows:

$$\dot{Q}_{conv\_inner,i,k} = 2\pi h R_{outer}(Ti - Tsi, k)/\theta_p, \tag{19}$$

where Tsi is the shell node j temperature of battery i, θ_p is the thermal resistance between the jellyroll and the battery shell. The thermal conductivity of separator is an order of magnitude smaller than other materials within the jellyroll [12], thus, θ_p can be estimated by the following equation:

$$\theta_p = tsep/(2\pi h R_{outer}\lambda sep), \tag{20}$$

where R_{outer} is the outer radius of the jellyroll, $tsep$ is the thickness of the separator, and λsep is the thermal conductivity of the separator.

For shell nodes, the energy equation considers the heat input (consisting of the quantity of heat transfer from jellyroll nodes to the shell nodes of thermal conduction), thermal conduction among the shell nodes and the heat output (consisting of the quantity of heat transfer from a battery to the circumstances of thermal conduction, thermal convection, and thermal radiation). It can be written as:

$$\rho_s C_{p,s} dTsi, k/dt = \sum_k (\dot{Q}_{conv\_inner,i,k} + \dot{Q}_{r,i,k} + \dot{Q}_{f,i,k}) + \sum_j \dot{Q}_{conv\_outer,i,j}, \tag{21}$$

where the terms ρ_{shell}, C_s, Ts are the average density, the total heat capacity, and the average temperature of battery shell, respectively. Based on the geometrical parameters of the batteries, $C_{p, jr}$ and the average density ρjr can be estimated by the following equations:

$$C_{p,s} = c_{p,shell}\rho_{shell} V_{shell}, \tag{22}$$

$$V_{shell} = A_{shell} \times h, \tag{23}$$

$$A_{shell}=2\pi(R_{outer} + R_{inner})L+2\pi R_{outer}^2, \tag{24}$$

$\dot{Q}_{f,i,k}$ is the radiation power of shell point k of battery i. $\dot{Q}_{conv\_outer,i,j}$ is the heat conduction power between battery i and battery j. Taking quadrilateral packing as an example. The related equations [12] are shown as follows:

$$\dot{Q}_{conv\_outer,i,j} = -(T_{si,k} - T_{sj,l})/\theta c, \tag{25}$$

$$\dot{Q}_f = -1/4 h_{conv}(T_{si,k} - T_{amb})A cell, \tag{26}$$

where $T_{si, k}$, $T_{sj, l}$ are the shell nodes temperatures of batteries i, j respectively; k, l represent specific nodes in battery shells. θc represents the total equivalent thermal transfer coefficient between the two adjacent batteries (K/W). It is calculated by a FEM model (Fig. 3). In this model, two steel pillars of width h with a semi-cylindrical face in on end are placed close together. A 100 W input heater is set in one end and a temperature boundary condition $T = T_{amb}$ in another end. The thermal resistance can be calculated by the equation shown in the Fig. 3. h_{conv} is the convection coefficient.

$\dot{Q}_{r,i,k}$ is the thermal radiation power. The thermal radiation can be calculated by the equation [12], as follows:

$$\dot{Q}_{r0,i,k} = \varepsilon\sigma(T_{si,k}^4 - T_{amb}^4)A cell, \tag{27}$$

where $\varepsilon=0.3$ [12], and $\sigma = 5.67 \times 10^{-8} Wm^{-2}K^{-4}$ is the Stefan–Boltzmann constant. $A cel$ is the surface area of the battery. According to the geometrical relationship, 1/6 of the thermal radiation heat can be absorbed by a neighboring battery based on the ideal assumption that the surface heat absorptivity of each battery is 1. For example, if $60° < \alpha \leq 90°$ (Fig. 2c), the rate of each node can be written as (consider the two-way effect of the radiation):

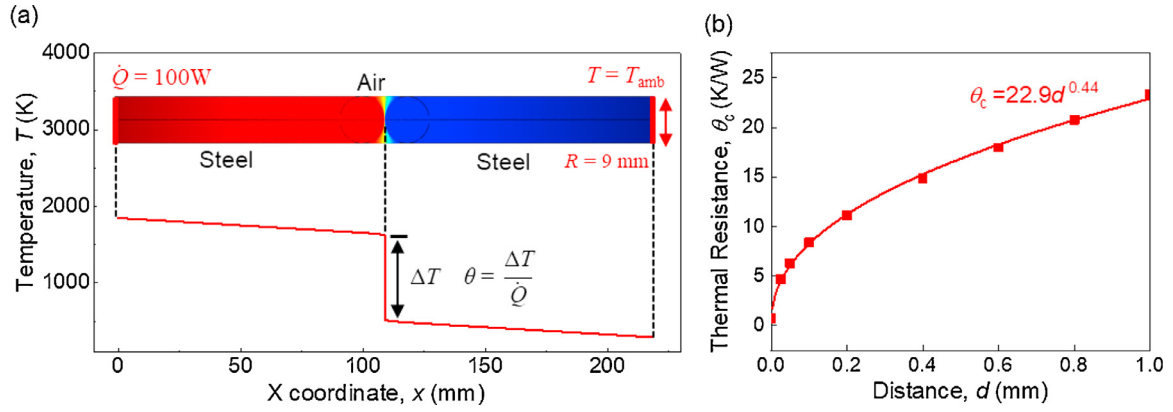$$\dot{Q}_{r,i,k} = \dot{Q}_{r0,i,k} - 2/3 \cdot \dot{Q}_{r,j,l}. \tag{28}$$

Fig. 3. Schematic illustration of the cylindrical surface contact resistance measurement. (a) Numerical experiment setup and calculation method of equivalent resistance; (b) Calculation results, the relationship between spacing and thermal resistance.

where $\dot{Q}_{r0,i,k}$ refers to the origin radiant energy emitted of battery i, shell node k and $\dot{Q}_{r,i,k}$ refer to the total radiant energy released after considering the two-way effect. are the surface temperatures of batteries i, j respectively; k, l represent specific nodes in battery shells.

The global ordinary differential and differential-algebraic equation component in software COMSOL Multiphysics are used to solve the model. The step time is set as adaptive. The relative tolerance is set by 10^{-5}. The total calculation time is 30 min ~ 60 min (4 cores).

3. Results and discussion

3.1. Experimental results and calibration of the model

Four experiments are conducted in this research. At first, the single battery case is to calibrate the model parameters of the TR model. The result suggests that the convective coefficient is set as 10 W/(m²K) (Fig. 4a).

A two-battery experiment is conducted to show the typical process of thermal propagation (Fig. 4b). When the runaway reaction of the first battery is triggered, its temperature increases dramatically to approximately 850 °C. Then, the temperature decreases due to thermal convection, conduction, and radiation. The temperature of the second battery increases rapidly as soon as the runaway reaction of the first battery is triggered. Such a phenomenon indicates that the runaway of the battery can be triggered when thermal propagation occurs in the neighborhood battery. The time interval ΔT between the two TR reactions of the cells is approximately 5 sec. Based on the infrared signal, the details of the thermal propagation are presented, which mainly contains five major stages,: (1) the internal short circuit of the first battery occurs; (2) the runaway reaction of the first battery is triggered; (3) the flame produced by the first battery starts to heat the neighborhood batteries; (4) the overheat of the local area causes the short circuit of the second battery, and its temperature increases dramatically; and (5) the runaway reaction of the second battery occurs, and a large number of gas blasts the battery case (Supplementary Material Video 1 (image signal) and Video 2 (infrared signal)). The battery shell fracture appears on the side near the neighboring battery due to the poor heat dissipation in the area between two batteries; thus, the accumulated thermal energy softens the battery case on the middle side.

When the size of the battery module is increased to 3 × 3, as shown in Fig. 4c, the duration of the thermal propagation is rather short, and the flame is also very intense as the video shown in Supplementary Material Video 3. According to the temperature curves, the thermal propagation process is exhibited. The schematic diagram indicates that runaway reactions of two batteries occur at the same time in some stages. The flame produced by the TR reaction triggered batteries is larger enough to lead to the ISC of batteries on a larger scale rather than the adjacent batteries.

Simulation results indicate that this model can predict the triggering runaway reaction of each battery well within a pack. Because of vibration and displacement caused by the fire and explosion on thermocouples, the middle part of the experimental curves has some jitters. Thus, some simulation curves, such as #2 in Fig. 4b, do not fit their experimental counterpart well. However, from the point of the onset of TR, the peak temperature, and the cooling process, the simulation results match the experimental results well (Table 1). For larger-scale battery packs, conducting the TR experiment is much more dangerous and expensive. Thus, the numerical model has more merits and significances to understand the thermal propagation mode and estimate the propagation speed within large battery packs in which the runaway experiments are very difficult to be conducted.

3.2. Thermal runaway propagation of large pack under ideal conditions

Based on the established validated model, a 20 × 20 battery pack is discussed. Battery spacing d is set as 0 mm, the packing angle α is 90°, the state of charge (SOC) is 100%, and the ambient temperature T_{amb} is 25 °C. The runaway reaction of the battery in the bottom left corner of a 20 × 20 battery pack is initially triggered. Approximately 86 s after the occurrence of the first runaway reaction, the TRs of all the batteries are triggered. Interestingly, the thermal propagation behaviors as a type of wave with a circular front during this process (Fig. 5a, Supplementary Material Video 4). Runaway reactions are propagated from each thermally triggered battery. The overall propagation front is their envelope. Simulation results also suggest that the speed of the front is approximately a const, defined as the spatial speed v_{TR}. And v_{TR} is a function of d (θ_c), T_{amb} and α. Based on these two rules, a concise thermal propagation theory is established. Here, the number of the TR triggered batteries is defined as N and the quantitative speed of the thermal propagation $\dot{N}$ within a pack is defined as the increased number of runaway reactions triggered batteries per unit time from the onset of the first runaway reaction to the last. According to geometric conditions, N can be written as

$$N = 8\rho_P (v_{TR}/D)^2 t^2, \tag{29}$$

where ρ_P is the packing density. For $d = 0$ mm, $\rho_P = 0.785$. Define $v = v_{TR}/D$ as the dimensionless propagation spatial speed. Thus, the dimensionless quantitative speed $\dot{N}$ can be written as

$$\dot{N} = 16\rho_P v^2 t \tag{30}$$

Based on the geometric relationship, the theoretical N–t curve is calculated, as shown in Fig. 5b. Furthermore, a simple equation can be applied to estimate the total time of the thermal propagation:

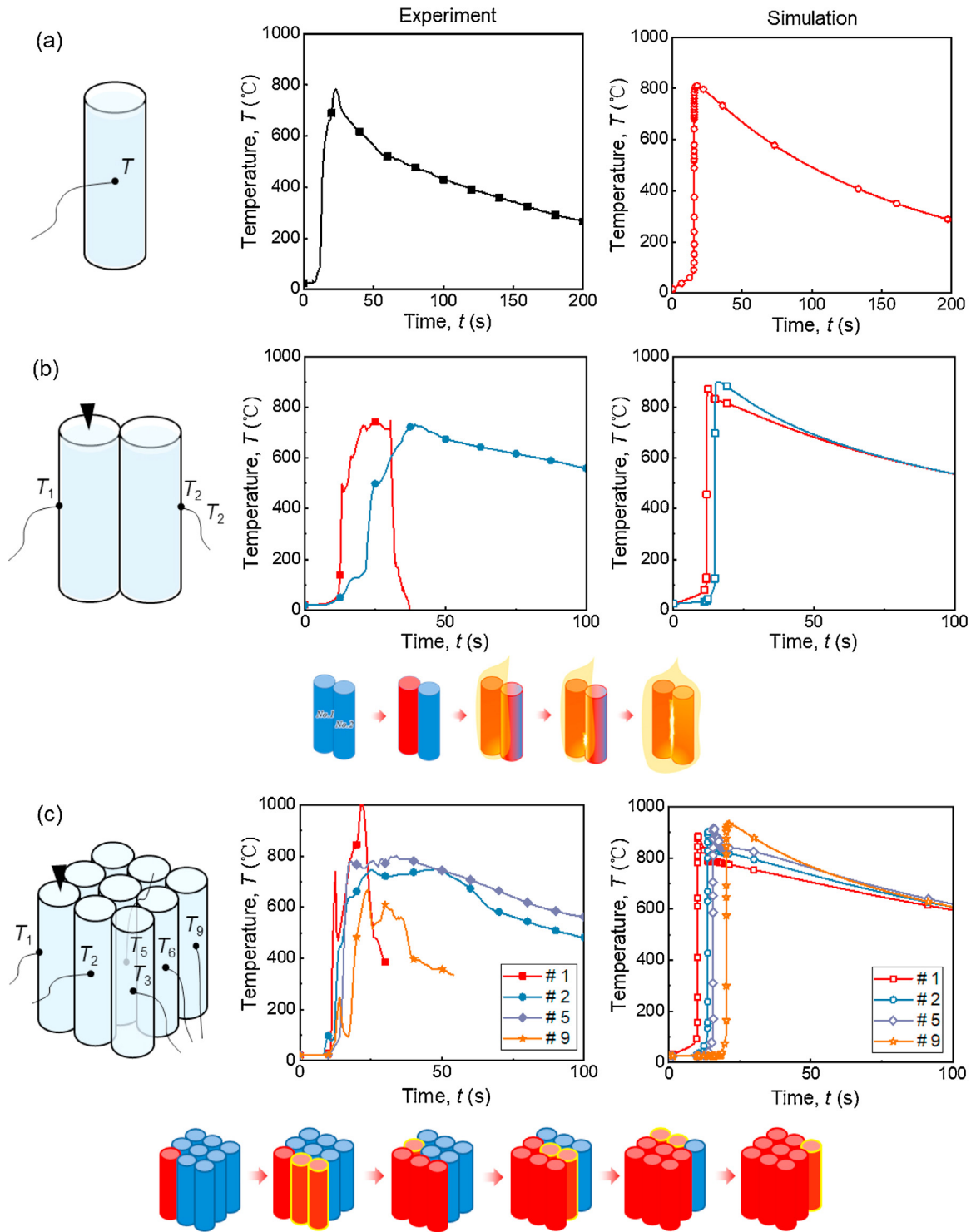$$T_{total} = \sqrt{(B-1)^2 + (H-1)^2}/v, \tag{31}$$

Fig. 4. Typical results of experiments and comparison between experiment and simulation. (a) single battery TR; (b) 1 × 2 pack TR; (c) 3 × 3 pack TR.

where B and L are the number of batteries in the width and length directions, respectively. D is the diameter of the battery. The estimation equation can be written in a more universal manner, as follows:

$$T_{total} = L/v, \tag{32}$$

where L is the nondimensionalized distance (actual distance normalized by battery diameter) between the first TR-triggered battery and the final TR-triggered battery. For example, when the initial TR is set inside the pack, the L should be the distance between the initial TR battery to the furthest battery within the pack (Fig. 5c, supplementary Material

Video 5). If the pack has an irregular shape, the TR propagation can be divided into several subprocesses. For example, the T-shaped battery pack's TR propagation can be divided into two subprocesses (Fig. 5d, supplementary Material Video 6).

For different packing angles, the TR propagation mode does not change. The propagation fronts are round (Supplementary Material Video 7). From a quantitative point of view, the TR propagation of the $\alpha = 60°$ pack is the fastest, the $\alpha = 75°$ pack is the slowest (Fig. 5e). For packs with $\alpha = 60°$, the TR propagation is slow at first but increases quickly and higher than packs with $\alpha = 90°$ The reason for the first slow

Table 1
Comparison of triggering time and temperature rise between experimental results and simulation results.

Case	#	Triggering time (s)			Temperature rise (°C)		
		Exp.	Sim.	Relative error rate	Exp.	Sim.	Relative error rate
2 batteries	1	12.75	11.821	−7.29%	721.61	846.18	17.26%
	2	22	14.761	−32.90%	711.37	874.96	23.00%
9 batteries	1	11	10.054	−8.60%	980.71	860.75	−12.23%
	2	12.5	13.618	8.94%	725.58	877	20.87%
	5	14.5	15.57	7.38%	781.69	890.72	13.95%
	9	18	20.2	12.22%	725.2	907.38	25.12%

propagation and finally quickly increasing are the same, the thermal contacts are 3/2 time more than the other two types of packs. For battery packs with $\alpha = 75°$, the thermal contact condition is the same as packs with $\alpha = 90°$, however, their packing density is low, and the heat dissipation area is larger.

3.3. Propagation modes and speed

Further research shows that battery spacing d affects the TR propagation speed significantly. Normally, the T_{total} of a two-battery pack at $d = 0$ mm is approximately 3 s (Fig. 6a, mode I). For another case at $d = 0.01$ mm, the T_{total} is prolonged to 18.2 s (Fig. 6b, mode II). The shape of the curves also changes. The essential difference between those two phenomena is their different θ_c values. Thus, two modes of TR propagation exist, based on the value of θ_c. The two modes are also found in experiments (the thermal images). Mode I: low θ_c leads to a

local overheating in the battery surface. The surface temperature exceeds the melting point of the separator quickly. The melting of the separator produces a local short circuit. This early-triggered ISC further accelerates TR triggering. Mode II: high θ_c prevents conductive heat from concentrating on the battery surface. The surface and jellyroll average temperatures converge over time. When the temperatures reach the T_{TR} (melting point of the separator), the TR will inevitably be triggered. The total time of TR propagation is significantly longer than that of Mode I. These results can be proven by the surface temperature curve (Fig. 6a). The simulation indicates that the threshold $\theta_c = 0.89$ K/W. Based on Mode II (d is set as 0.01 mm, $\theta_c = 2.94$ W/K), the TR propagation front tends to be quadrate in a 90° pack (Fig. 6b, supplementary Material Video 8). In a 60° packing scenario, similar results are obtained by the model. The TR propagation front tends to be a hexagon (Fig. 6c, supplementary Material Video 9).

For Mode II, batteries are mainly heated by the surrounding TR-triggered batteries before their TRs are triggered. In this case, the batteries inside are heated by two batteries at the same time. Their TRs are triggered more quickly along the direction perpendicular to the front compared with that along the front (Fig. 6b–c). However, for Mode I, batteries are heated by surrounding batteries and themselves due to their early-triggered ISC. Thus, the differences among the TR propagation speeds in all directions are not obvious in this case.

In general, the spatial speed as the function of spacing $d(K)$, and ambient temperature T_{amb} can be written as

$$v = f(d, T_{amb}) = f(K, T_{amb}) = f(K', T') \qquad (33)$$

where $K' = K/K(d = 0mm)$ is the normalized equivalent thermal
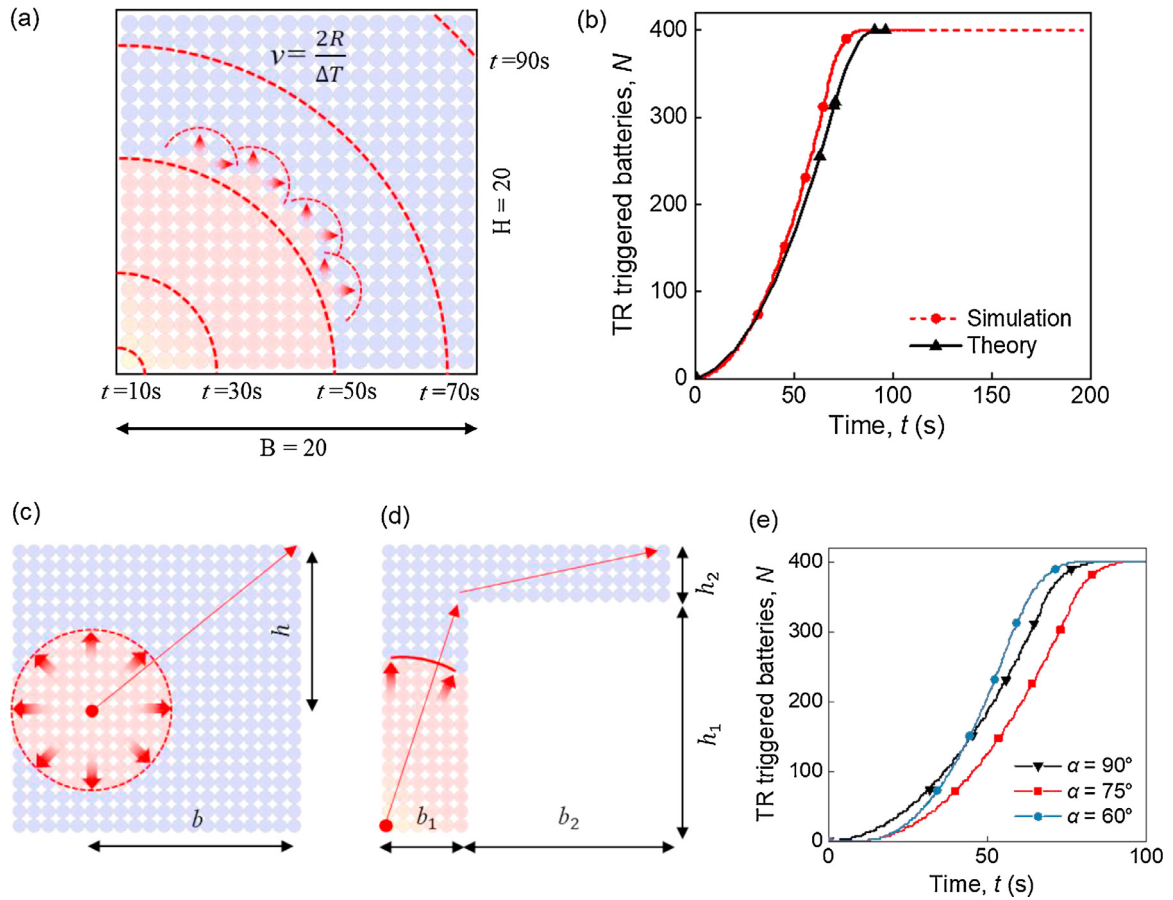

Fig. 5. Typical results of the TR of a 20 × 20 ideal thermal contact pack and the estimation method of the total TR propagation time. (a) propagation direction and speed; (b) comparison between theoretical curve calculated by the propagation theory and numerical calculation curve; (c) estimation method for the situation in which the first TR is triggered inside; (d) estimation method for T shape packs; (e) propagation speeds at different packing angles. (For interpretation of the references to colour in this figure legend, the reader is referred to the web version of this article.)
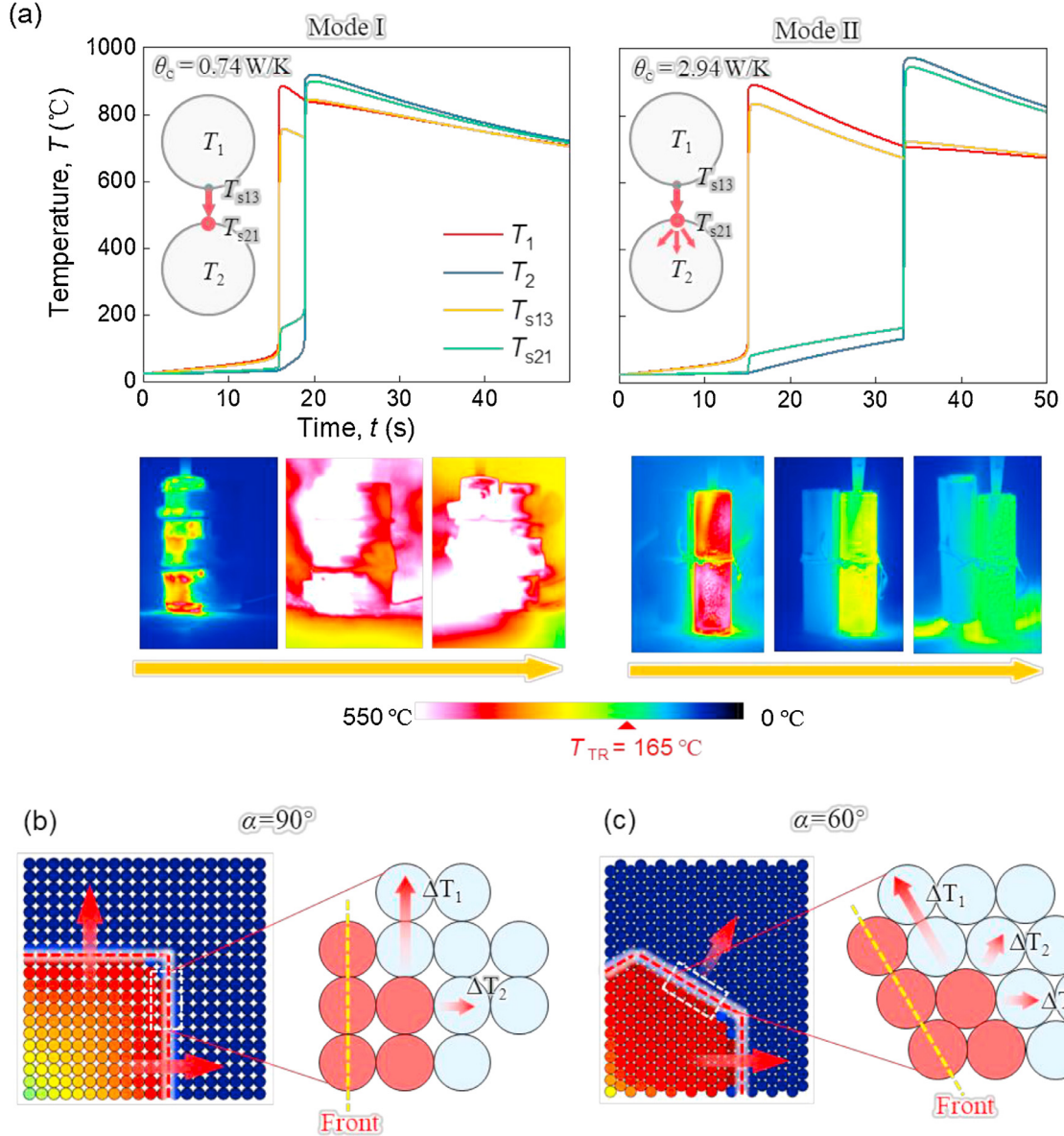
Fig. 6. Typical phenomena and mechanisms of TR propagation when thermal contact changes. (a) simulation results: 1×2 pack ($K = 1.35$ W/ °C (or $d = 0$ mm) and $K = 0.34$ W/ °C (or $d = \sim 0.01$ mm)); (b) propagation front of pack at $\alpha = 90°$ under mode II; (c) propagation front of pack at $\alpha = 60°$ under mode II.

transfer coefficient, T' is the thermodynamic temperature.

Through parametric calculation, the following empirical formula can be obtained

$$v = 1.62 \left(0.52 + 2.04 \times 10^{-6} e^{0.036 T'} \right) (0.62 K'^{0.56}) \tag{34}$$

The dimensionless propagation spatial speed v with d between $0\sim1$ mm and ambient temperature between -20 °C$\sim$90 °C can be presented as Fig. 7 shown Consider the relationship between spacing and thermal resistance,

$$K = 1/\theta_c = 1/(22.4 d^{0.44}) \tag{35}$$

First, the TR propagation speed increases with T_{amb}, because a high T_{amb} corresponds to a high initial thermal energy within each battery. Second, the TR propagation speed increases when battery spacing d decreases. Decreasing d means decreasing the equivalent thermal resistance. The lower the thermal resistance, the quicker the heat transfer. The d, T_{amb} decide together if TR propagation occurs, and its propagation speed (Fig. 7).

3.4. Thermal runaway propagation under random thermal conditions

For actual battery packs, the thermal contact condition cannot be very even. Besides, the fire or explosion during the TR process, the thermal resistance or heat transfer coefficient may change. For example, the fire of a TR trigged battery could also heat the sounding batteries expect for the thermal conduction and the thermal radiation. The equivalent heat transfer coefficient becomes large. Also, the explosion of a battery may push the surrounding batteries away. The equivalent heat transfer coefficient becomes smaller. Thus, battery packs with random equal heat transfer coefficients ($K = 1/\theta_c$) between 0 W/K and 2.7 W/K were constructed. The average value of 1.35 W/K is the same as the battery packs with $d = 0$ mm and $\alpha = 90°$ discussed above. Simulation results show that the TR propagations of the battery packs with random thermal coefficients are stable and little slower than the battery packs with even thermal coefficients (Fig. 8a). Due to the uneven thermal contact condition, the TR cannot always propagation along a straight line, the spatial speed decreases (Fig. 8b, supplementary Material Video 10).
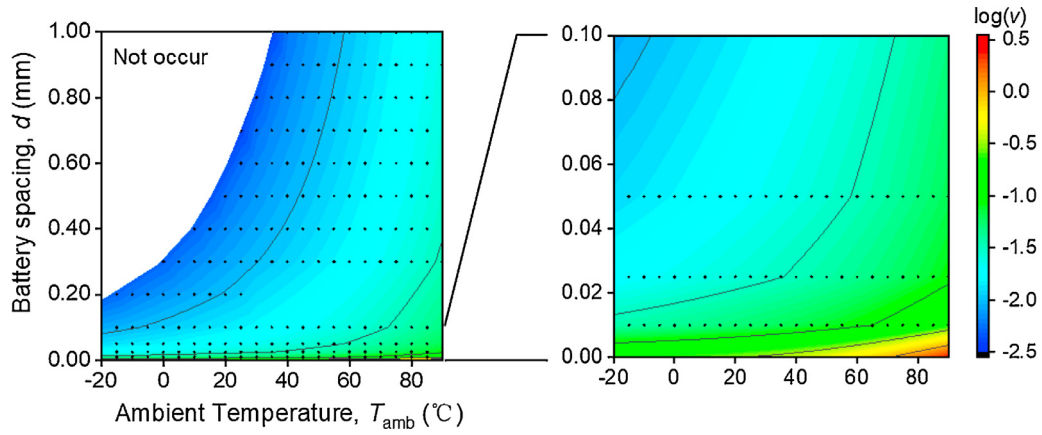
Fig. 7. Schematic of the coupling effect of battery spacing and ambient temperature on TR propagation speed. The value log(v) is used to indicate the TR propagation spatial speed. v is the propagation spatial speed and D is the diameter of the battery.

4. Conclusions

In summary, the behavior and mechanisms of thermal runaway propagation within a battery pack are unlocked by a series of experiments and a TR propagation computational model. The experiments are conducted by mechanically triggering the TR of a specific-location battery in battery packs of various sizes. The computational model is established by combining the 0D TR, electrical, and thermal conduction models. Two typical modes of TR propagation are discovered, and their mechanisms are further provided through simulation.

- Mode I: under low θ_c, a local overheating in the battery surface produces a local short circuit. This early-triggered ISC further accelerates the TR triggering.
- Mode II: under high θ_c, conductive heat cannot concentrate on the battery surface. The surface and jellyroll average temperatures converge over time. When the temperatures reach the T_{TR}, the TR will be triggered inevitably. The total time of TR propagation is significantly longer than that of Mode I. The batteries are mainly heated to T_{TR} by their surrounding TR-triggered batteries.

Within a large pack, the TR propagation front is approximately a circle based on Mode I, whereas it is a regular polygon based on Mode II. Numerical computation indicates that small packing space and high ambient temperature can increase the speed of TR propagation. Results provide theoretical insights into the fundamental understanding of TR propagation within battery packs of LIBs along with an efficient and effective computational frame for the safe design of battery packs.

Nonetheless, the simulation methods were idealized or simplify the calculation in this study. To accurately simulate a specific battery pack of an electric vehicle, more detail and difficult effects, such as the effect of fire and explosion, the effect of the cooling system, the effect of battery shape, should be further studied.

CRediT authorship contribution statement

Yikai Jia: Methodology, Data curation, Visualization, Writing - original draft. **Mesbah Uddin:** Data curation, Writing - review & editing. **Yangxing Li:** Conceptualization, Validation, Writing - review & editing. **Jun Xu:** Conceptualization, Supervision, Methodology, Data curation, Writing - review & editing.

Declaration of Competing interest

The authors declare that they have no known competing financial interests or personal relationships that could have appeared to influence the work reported in this paper.

Supplementary materials

Supplementary material associated with this article can be found, in the online version, at doi:10.1016/j.est.2020.101668.
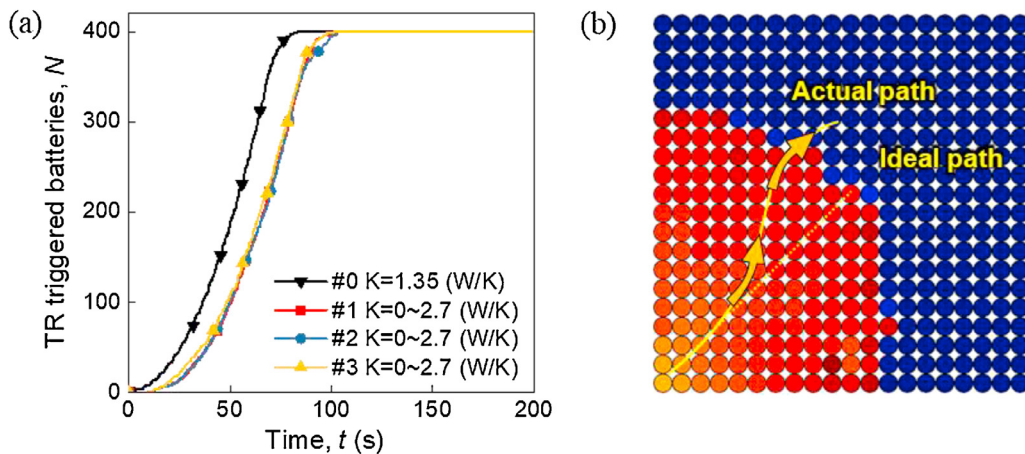

Fig. 8. TR propagations under conditions with random thermal contacts among batteries. The equivalent thermal transfer coefficients are set as random between 0 W/K to 2.7 W/K (a) N–t curves and (b) their related possible propagation path.

References

[1] T. Hatchard, D. D. MacNeil, A. Basu, J. R. Dahn, Thermal Model of Cylindrical and Prismatic Lithium-Ion Cells, J Electrochem Soc 148 (2001) A755–A761, https://doi.org/10.1149/1.1377592.

[2] P.T. Coman, E.C. Darcy, C.T. Veje, R.E. White, Modelling Li-Ion Cell Thermal Runaway Triggered by an Internal Short Circuit Device Using an Efficiency Factor and Arrhenius Formulations, J Electrochem Soc 164 (2017) A587–A593, https://doi.org/10.1149/2.0341704jes.

[3] G.-.H. Kim, A. Pesaran, R. Spotnitz, A three-dimensional thermal abuse model for lithium-ion cells, J Power Sources 170 (2007) 476–489, https://doi.org/10.1016/j.jpowsour.2007.04.018.

[4] A.W. Golubkov, D. Fuchs, J. Wagner, H. Wiltsche, C. Stangl, G. Fauler, et al., Thermal-runaway experiments on consumer Li-ion batteries with metal-oxide and olivin-type cathodes, RSC Adv 4 (2014) 3633–3642, https://doi.org/10.1039/C3RA45748F.

[5] B. Liu, Y. Jia, J. Li, S. Yin, C. Yuan, Z. Hu, et al., Safety issues caused by internal short circuits in lithium-ion batteries, Journal of Materials Chemistry A 6 (2018) 21475–21484, https://doi.org/10.1039/C8TA08997C.

[6] J. Zhu, T. Wierzbicki, W. Li, A review of safety-focused mechanical modeling of commercial lithium-ion batteries, J Power Sources 378 (2018) 153–168, https://doi.org/10.1016/j.jpowsour.2017.12.034.

[7] B. Liu, Y. Jia, C. Yuan, L. Wang, X. Gao, S. Yin, et al., Safety issues and mechanisms of lithium-ion battery cell upon mechanical abusive loading: a review, Energy Storage Materials 24 (2020) 85–112, https://doi.org/10.1016/j.ensm.2019.06.036.

[8] Y. Jia, S. Yin, B. Liu, H. Zhao, H. Yu, J. Li, et al., Unlocking the coupling mechanical-electrochemical behavior of lithium-ion battery upon dynamic mechanical loading, Energy 166 (2019) 951–960 doi:10.1016/j.energy.2018.10.142.

[9] J. Xu, Y. Jia, B. Liu, H. Zhao, H. Yu, J. Li, et al., Coupling Effect of State-of-Health and State-of-Charge on the Mechanical Integrity of Lithium-Ion Batteries, Exp Mech 58 (2018) 633–643, https://doi.org/10.1007/s11340-018-0380-9.

[10] L. Wang, S. Yin, J. Xu, A detailed computational model for cylindrical lithium-ion batteries under mechanical loading: from cell deformation to short-circuit onset, J Power Sources 413 (2019) 284–292, https://doi.org/10.1016/j.jpowsour.2018.12.059.

[11] Y. Jia, B. Liu, Z. Hong, S. Yin, D.P. Finegan, J. Xu, Safety issues of defective lithium-ion batteries: identification and risk evaluation, Journal of Materials Chemistry A (2020), https://doi.org/10.1039/D0TA04171H.

[12] P. Huang, P. Ping, K. Li, H. Chen, Q. Wang, J. Wen, et al., Experimental and modeling analysis of thermal runaway propagation over the large format energy storage battery module with Li4Ti5O12 anode, Appl Energy 183 (2016) 659–673, https://doi.org/10.1016/j.apenergy.2016.08.160.

[13] H. Wu, D. Zhuo, D. Kong, Y. Cui, Improving battery safety by early detection of internal shorting with a bifunctional separator, Nat Commun 5 (2014) 5193, https://doi.org/10.1038/ncomms6193.

[14] P. Bai, J. Li, F.R. Brushett, M.Z. Bazant, Transition of lithium growth mechanisms in liquid electrolytes, Energy Environ Sci 9 (2016) 3221–3229, https://doi.org/10.1039/C6EE01674J.

[15] Q. Wang, P. Ping, X. Zhao, G. Chu, J. Sun, C. Chen, Thermal runaway caused fire and explosion of lithium ion battery, J Power Sources 208 (2012) 210–224, https://doi.org/10.1016/j.jpowsour.2012.02.038.

[16] T.M. Bandhauer, S. Garimella, T.F. Fuller, A Critical Review of Thermal Issues in Lithium-Ion Batteries, J Electrochem Soc 158 (2011) R1–R25, https://doi.org/10.1149/1.3515880.

[17] B. Liu, J. Zhang, C. Zhang, J. Xu, Mechanical integrity of 18650 lithium-ion battery module: packing density and packing mode, Eng Fail Anal 91 (2018) 315–326, https://doi.org/10.1016/j.engfailanal.2018.04.041.

[18] B. Liu, H. Zhao, H. Yu, J. Li, J. Xu, Multiphysics computational framework for cylindrical lithium-ion batteries under mechanical abusive loading, Electrochim. Acta 256 (2017) 172–184, https://doi.org/10.1016/j.electacta.2017.10.045.

[19] C. Yuan, L. Wang, S. Yin, J. Xu, Generalized separator failure criteria for internal short circuit of lithium-ion battery, J Power Sources 467 (2020) 228360, , https://doi.org/10.1016/j.jpowsour.2020.228360.

[20] J. Weng, X. Yang, D. Ouyang, M. Chen, G. Zhang, J. Wang, Comparative study on the transversal/lengthwise thermal failure propagation and heating position effect of lithium-ion batteries, Appl Energy 255 (2019) 113761, , https://doi.org/10.1016/j.apenergy.2019.113761.

[21] Y. Jia, J. Xu, Modeling of Thermal Propagation Based on Two Cylindrical Lithium-Ion Cells, Journal of Electrochemical Energy Conversion and Storage 17 (2019), https://doi.org/10.1115/1.4045199.

[22] D. Ouyang, J. Weng, J. Hu, M. Chen, Q. Huang, J. Wang, Experimental investigation of thermal failure propagation in typical lithium-ion battery modules, Thermochim Acta 676 (2019) 205–213, https://doi.org/10.1016/j.tca.2019.05.002.

[23] M. Chen, O. Dongxu, J. Liu, J. Wang, Investigation on thermal and fire propagation behaviors of multiple lithium-ion batteries within the package, Appl Therm Eng 157 (2019) 113750, , https://doi.org/10.1016/j.applthermaleng.2019.113750.

[24] C. Lee, A.O. Said, S.I. Stoliarov, Impact of State of Charge and Cell Arrangement on Thermal Runaway Propagation in Lithium Ion Battery Arrays, Transp Res Rec 2673 (2019) 408–417, https://doi.org/10.1177/0361198119845654.

[25] L. Wang, X. Duan, B. Liu, Q.M. Li, S. Yin, J. Xu, Deformation and failure behaviors of anode in lithium-ion batteries: model and mechanism, J Power Sources (2019) 227468, , https://doi.org/10.1016/j.jpowsour.2019.227468.

[26] S. Gao, L. Lu, M. Ouyang, Y. Duan, X. Zhu, C. Xu, et al., Experimental Study on Module-to-Module Thermal Runaway-Propagation in a Battery Pack, J Electrochem Soc 166 (2019) A2065–A2073, https://doi.org/10.1149/2.1011910jes.

[27] F. Larsson, J. Anderson, P. Andersson, B.E. Mellander, Thermal Modelling of Cell-to-Cell Fire Propagation and Cascading Thermal Runaway Failure Effects for Lithium-Ion Battery Cells and Modules Using Fire Walls, J Electrochem Soc 163 (2016) A2854–A2865, https://doi.org/10.1149/2.0131614jes.

[28] J. Lamb, C.J. Orendorff, L.A.M. Steele, S.W. Spangler, Failure propagation in multi-cell lithium ion batteries, J Power Sources 283 (2015) 517–523, https://doi.org/10.1016/j.jpowsour.2014.10.081.

[29] C. F. Lopez, J. A. Jeevarajan, P. P. Mukherjee, Experimental Analysis of Thermal Runaway and Propagation in Lithium-Ion Battery Modules, J Electrochem Soc 162 (2015) A1905–A1915, https://doi.org/10.1149/2.0921509jes.

[30] X. Feng, L. Lu, M. Ouyang, J. Li, X. He, A 3D thermal runaway propagation model for a large format lithium ion battery module, Energy 115 (2016) 194–208, https://doi.org/10.1016/j.energy.2016.08.094.

[31] X. Feng, X. He, M. Ouyang, L. Lu, P. Wu, C. Kulp, et al., Thermal runaway propagation model for designing a safer battery pack with 25Ah LiNixCoyMnzO2 large format lithium ion battery, Appl Energy 154 (2015) 74–91, https://doi.org/10.1016/j.apenergy.2015.04.118.

[32] H. Zhou, Z. Yang, D. Xiao, K. Xiao, J. Li, An electrolyte to improve the deep charge–discharge performance of LiNi 0.8 Co 0.15 Al 0.05 O 2 cathode, J. Mater. Sci. Mater. Electron. 29 (2018) 1–12, https://doi.org/10.1007/s10854-018-8650-y.

[33] R.M. Spotnitz, J. Weaver, G. Yeduvaka, D.H. Doughty, E.P. Roth, Simulation of abuse tolerance of lithium-ion battery packs, J Power Sources 163 (2007) 1080–1086, https://doi.org/10.1016/j.jpowsour.2006.10.013.

[34] H. Maleki, A.K. Shamsuri, Thermal analysis and modeling of a notebook computer battery, J Power Sources 115 (2003) 131–136, https://doi.org/10.1016/S0378-7753(02)00722-X.

[35] G.H. Kim, A. Pesaran, R. Spotnitz, A three-dimensional thermal abuse model for lithium-ion cells, J Power Sources 170 (2007) 476–489, https://doi.org/10.1016/j.jpowsour.2007.04.018.

[36] D.M. Carrera, M. G. Quantum Tunneling in Chemical Reactions 2007.

[37] M. Ouyang, M. Zhang, X. Feng, L. Lu, J. Li, X. He, et al., Internal short circuit detection for battery pack using equivalent parameter and consistency method, J Power Sources 294 (2015) 272–283, https://doi.org/10.1016/j.jpowsour.2015.06.087.

[38] P. Coman, S. Rayman, R. E White, A lumped model of venting during thermal runaway in a cylindrical Lithium Cobalt Oxide lithium-ion cell, J Power Sources 307 (2016) 56–62, https://doi.org/10.1016/j.jpowsour.2015.12.088.

[39] X. Feng, D. Ren, X. He, M. Ouyang, Mitigating Thermal Runaway of Lithium-Ion Batteries, Joule 4 (2020) 28, https://doi.org/10.1016/j.joule.2020.02.010.

[40] P.T. Coman, E.C. Darcy, C.T. Veje, R.E. White, Numerical analysis of heat propagation in a battery pack using a novel technology for triggering thermal runaway, Appl Energy 203 (2017) 189–200, https://doi.org/10.1016/j.apenergy.2017.06.033.

[41] R. Zhao, J. Liu, J. Gu, Simulation and experimental study on lithium ion battery short circuit, Appl Energy 173 (2016) 29–39, https://doi.org/10.1016/j.apenergy.2016.04.016.